Microwave response phase control of a graphite microstrip

Arsen Babajanyan [a, *], Tigran Abrahamyan [a], Hovhannes Haroyan [a], Billi Minasyan [a], Torgom Yezekyan [b], Kiejin Lee [c], Barry Friedman [d], Khachatur Nerkararyan [a]

[a] Department of Radiophysics, Yerevan State University, Yerevan, 0025, Armenia
[b] Center for Nano Optics, Southern Denmark University, Odense, 5230, Denmark
[c] Department of Physics, Sogang University, Seoul, 121-742, South Korea
[d] Department of Physics, Sam Houston State University, Huntsville, TX, 77341, USA

ARTICLE INFO

ABSTRACT

Interaction between a carbon based low-conductivity graphite microstrip, which is an element of a metamaterial, and incident electromagnetic (EM) waves was investigated in the microwave range of frequency (8–12 GHz). The distribution of the magnetic near-field visualized by a non-contact thermoelastic optical indicator microscope, has three localization centers which vary significantly depending on the conductivity of the graphite microstrip. In the case of high resistance, the EM field was mostly localized near the microstrip. With decrease of resistance, new localization zones of EM field were formed, the intensity of which was constantly increased, and continuously decreased near the microstrip. Analysis of images resulting from the superposition of incident and scattered waves reveals a significant increase in the scattered wave phase-shift due to an increase in the conductivity of the graphite microstrip. A metamaterial consisting of elements with such regulated conductivity can serve as a phase-tuning system for radiation control.

© 2022 Elsevier Ltd. All rights reserved.

1. Introduction

Metamaterials and metasurfaces are currently in the focus of a wide range of researchers. Metamaterials are artificial media in which the propagation properties of the electromagnetic (EM) wave are mainly defined by their underlying structures with the feature size much smaller than the operational wavelength [1–4]. Metasurfaces are the two-dimensional counterparts of metamaterials, composed of discrete subwavelength structures in an ultrathin film at the interface and possessing the capability of full control of light properties in terms of amplitude, phase, dispersion, momentum and polarization [5–8].

These newly invented devices have attracted enormous attention for their versatile functionality, ultra-thin features, and ease for integration compared with conventional refractive optics. There has been intensive research on different types of metasurfaces such as frequency selective metasurfaces [9–11], high impedance metasurfaces [12,13], perfectly absorbing metasurfaces [14,15], and wave-front shaping metasurfaces [16–18].

As a matter of fact, the evidence of different physical processes in metasurfaces is not only a consequence of structural peculiarities, but also of the physical properties of the basic structural element (so called meta-molecule or meta-element). Usually the choice of the meta-molecule is dictated by the possibilities of controlling Ohmic losses [8]. Thus, to control the intensity and polarization of transmitted and scattered radiation it is desirable to minimize the Ohmic losses and vice versa, i.e. to have an efficient absorbing layer one needs to increase them.

In such complicated systems, the evidence of predictable results should be accomplished by a precise investigation, which can be achieved by assuming certain simplifications. Therefore, usually the ratio of real and imaginary parts of dielectric constant of the media which is forming the meta-elements is either extremely larger or infinitesimally smaller than one. Nevertheless, going beyond these limitations may lead to new effects, which will improve the understanding of the meta-element properties and metasurfaces in general. However, further, development has shown that the unique properties of meta-elements do not disappear when the three-dimensional (3D) structures are replaced by similar thin-films, which provides more favorable conditions in terms of application.

From this prospective of view, carbon based composite materials are one of most promising structure for the basic meta-

elements of metamaterials in the microwave [19] and terahertz [20] ranges. However, there are technological and functional difficulties in designing of tunable metamaterials for better dynamic control of EM polarization and manipulation in the broadband ranges.

To obtain an effective phase shifting in the microwave range, two conditions must be realized. First, the real and imaginary parts of effective dielectric permittivity of the microstrip must be of the same magnitude [21]. From this point of view, the choice of carbon mixture materials is highly expedient. Numerous measurements show that the real and imaginary parts of the dielectric permittivity of the carbon composites, depending on the components proportion, can be varied over a fairly wide range [21—26]. Next, a significant change of one of these quantities should not lead to a significant change of the other. This can be realized in the percolation transition state of the composite material, where the real part of the effective dielectric permittivity does not change in practice [27—29].

In this manuscript, a characteristic of interaction between a carbon based low-conductivity graphite microstrip (with thickness smaller than the skin-depth) which is an element of a metamaterial and linearly polarized microwaves was investigated by experimental and numerical simulation methods. The aim is to determine the capabilities of the EM field amplitude and phase control formed in their vicinity. This will allow to control of the phase-matched coupling between conductive elements of metamaterials in the microwave range; determining the most favorable configurations of metamaterials to ensure optimal absorption, focusing, and beam steering.

2. Materials and methods

2.1. TEOIM method

Fig. 1 shows the schematic of the experimental setup. Microwave magnetic near-field (MMNF) visualization was carried out by a thermoelastic optical indicator microscope (TEOIM). The TEOIM is based on the rotation of light polarization due to the linear birefringence (LB) of the medium caused by a conversion of the heat source distribution to the thermal stress distribution in the optical indicator (OI) (due to photoelastic effect). The measurement principle of the optical part of the experimental setup is based on the polarized light microscope system [30].
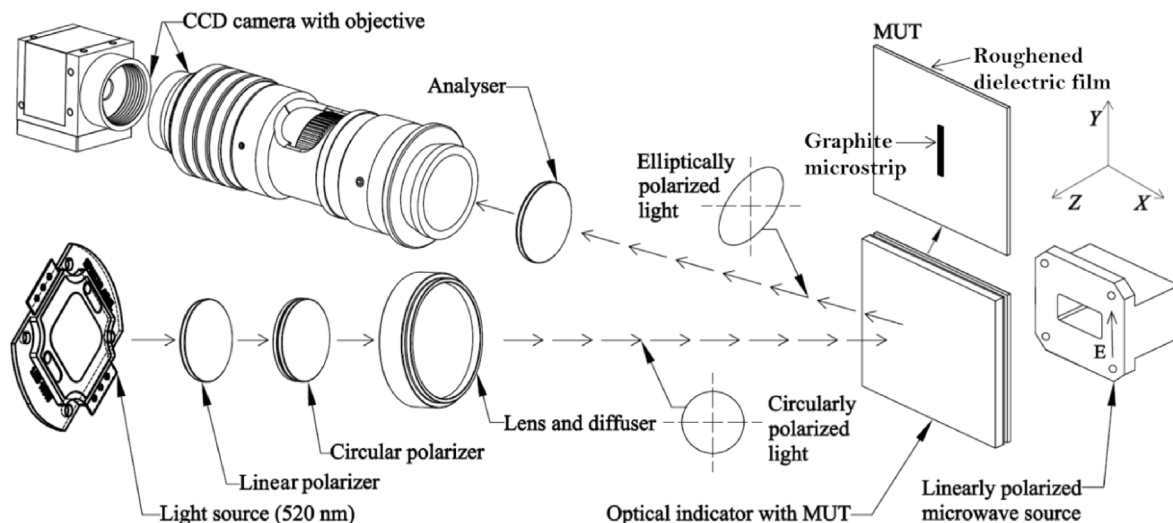
Experimental setup consists of two principal parts: the optical part, where the change of the polarization state is measured and the microwave part, where an OI illuminated with microwaves acts as a heat source. The microwave radiation was generated by synthesized sweeper R&S SMA100B, amplified by a microwave power amplifier Mini-Circuits ZVE-3W-183+ (0—35 dBm) and then transmitted to the rectangular waveguide Pasternak WR-90. The generated microwave signal frequency was in the range of 8—12 GHz and the intensity was controlled (up to 1 W). The waveguide is directed to the OI. In the optical part of the setup, the emitted green light (LED, $\lambda \approx 520$ nm) becomes circularly polarized by passing through a linear sheet polarizer and circular polarizer (λ/4 wave-plate). After reflection from the OI, the incident circular polarized light changes its polarization to elliptical due to the photoelastic effect; then passing through to the analyzer is registered by the CCD camera with 1024×768 resolution. The CCD camera measures the change of the polarization state of the reflected light from a change of the intensity of the reflected light by detecting the LB distribution images for two different orientations of the analyzer: 0° and 45°.

Solving the reverse problem by measuring the change of intensity of the reflected light it is possible to find the EM field distribution in the OI. The working principle of TEOIM setup, software program application, and image processing were described in detail in Ref. [30].

In general, the optical indicators are composed of a glass substrate coated by a conductive thin-film for absorbing the heat or EM fields. In our case, the OI is Indium-tin-oxide (ITO) which is designed for heat-transfer due to the magnetic field absorption [31,32]. As the ITO is very thin (180 nm), the system records the tangential (in-plane) component of the MMNF.

2.2. Fabrication of graphite microstrips

In the experiment, the material under test (MUT) was a metamaterial element: a polyethylene film with a surface roughness of $Th = 20$ μm was used as a substrate. The surface was smoothed with Koh-I-Noor Hardmuth 8B type graphite pencil and the mass amount of the mixture is follow: 90% graphite, 4% clay, and 5% wax. The length and the width of the formed graphite microstrip was $L = 2$ cm length and $W = 2$ mm, respectively. In the final leveling step, the sample resistance changed to 0.6—3.0 KOhm when adding a

Fig. 1. The schematic of the experimental setup, MUT, and the microwave source.

layer of graphite mixture up to 2 μm. The resistances of fabricated graphite microstrips were measured by a LCR bridge R&S HM8118.

The final selection of the MUT was made by combining experimental-numerical calculation data, approaching the optimal parameters step by step. The required results are obtained when a significant change in the imaginary part of the dielectric permittivity (i.e., the conductivity) of the MUT does not lead to a significant change in its real part. This is realized by the percolation transition process, which in this case is possible by deposition of a mixture of graphite and resin (clay and wax) on a rough dielectric surface [27—29]. Thus, by choosing the mixture combination, as well as the characteristic size of the surface roughness, the optimal parameters of the MUT are obtained. The investigated phenomenon is observed in the final stage of leveling the graphite surface. The value of the real part of the effective dielectric permittivity ($\varepsilon_r = 500$) of the graphite microstrip in the 8—12 GHz range was chosen to ensure agreement of the experimental and simulation results.

The MUT was attached to a ceramic plate with a thickness of 1 mm and placed between the microwave source and OI. The MUT was directed to the microwave source by the microstrip side. The distance between the OI and rectangular waveguide (i.e. microwave radiation source) was 5 mm. Note that, the incident microwave field pattern (distribution the in x-y plane) has Gaussian behavior starting from 2 mm from the end of the waveguide, thus we can assume that on the MUT the microwaves were incident with the Gaussian form. In the experiment the ceramic plate provides a homogenous and monochrome view of reflected light in a visible area of the camera. The MMNF in-plane component was visualized for MUTs with different resistances.

2.3. Computer simulation of experiment

EM field distributions around the MUT were investigated through a 3D full-wave numerical analysis using the COMSOL Multiphysics software based on the finite element method. A Gaussian beam was used as a source of radiation, while size and the properties of the graphite microstrip were chosen mainly according to the experiment, though for the microstrip conductivity we used static characteristics, implying that in the microwave region of the frequencies we used, they will be identical. The system is enclosed by a box with the scattering boundary conditions applied to its walls. The phase matched layer was added to the external boundaries of the surrounding medium, which eliminate any reflection or scattering from the external boundaries. These boundary conditions with large enough box sizes (triple of the operating wavelength) prevent the influence of the back-scattered waves from the boundaries and imitate free space.

3. Results and discussions

3.1. EM field visualization

The linearly polarized microwave beam was incident on the MUT normally. The visualized distribution of MMNF for 11 GHz at a distance of 1 mm from MUT is shown in Fig. 2. Here, the experimental results are presented in Fig. (a—f). In particular, Fig. 2 (a) shows the distribution of measured incident linear polarized MMNF with a 1 W intensity at 11 GHz (i.e. without MUT). Fig. 2(b—f) shows the distribution of measured MMNF for MUT with (b) 3.0 KOhm, (c) 1.3 KOhm, (d) 1.0 KOhm, (e) 0.8 KOhm, and (f) 0.6 KOhm DC resistances. The grey solid rectangles are the contours of the graphite microstrips. The simulation results are presented in Fig. (g—l). In particular, Fig. 2 (g) shows the distribution of measured incident linear polarized MMNF with a 1 W intensity at 11 GHz (i.e. without MUT). Fig. 2(h—l) shows the distribution of measured

MMNF for MUT with (h) 10 S/m, (i) 60 S/m, (j) 80 S/m, (k) 120 S/m, and (l) 250 S/m conductivities. Again, the grey solid rectangles are the contours of the graphite microstrips. The values of conductivities and the real part of effective dielectric permittivity ($\varepsilon_r = 500$) of the graphite microstrip, were chosen to ensure agreement of the experimental and simulation results. The comparison of experimental and simulation data is given in Fig. 2(m—r), where the cross-sectional profiles for measured and simulated MMNF images along white solid lines are compared. Note that according to the presented data, the conductivity in the microwave range is about one order of magnitude smaller than the DC conductivity.

For the given parameters, the thickness of the graphite microstrip with low conductivity is significantly less than the thickness of the skin depth, and the MUT area is significantly smaller than the cross-sectional area of the incident microwaves, thus the MMNF was formed by superposition of incident and scattered wave fields.

The analysis of the obtained images shows that the distribution of the MMNF has three localization centers which vary significantly depending on the conductivity of the sample. In the case of small conductivity (<100 S/m) the field was mostly localized near the microstrip. With the increase of microstrip conductivity (>150 S/m), new localization zones of field were formed on the sides of microstrip with constantly increased intensities, while it decreased near the microstrip. These features shown in the images are also clearly seen in the cross-sectional profiles (Fig. 2(m—r)) both for experimental and simulation data. Note that during the growth of conductivity, the position of the newly formed centers of intensity does not essentially change, and the distance between them is significantly greater than the width of the microstrip (about 10 times) as shown in Fig. 2(c—f) and Fig. 2(i—l).

The frequency-dependent behaviors of visualized intensity for MMNF both for experimental and simulated data (data are not shown here) show that the incident MMNF without MUT has a circular shape which refers to the fundamental mode of the rectangular waveguide used as a source of all radiated frequencies (8—12 GHz). The images for the MUTs with different resistances (0.6—3.0 KOhm) showed that MUT strongly interacts with the microwave radiation and absorbs a part of energy in this frequency range. The dependences of the normalized intensity of the MMNF on frequency without and with the MUTs demonstrate an almost linear behavior with $\Delta I/\Delta f = 0.2$ GHz^{-1} of slope and $R^2 = 0.96$. 11 GHz was chosen as an optimal frequency for the investigations because of the experimental configuration limited by the optimal operating frequency range of the waveguide (8—12 GHz), OI, and peculiarities of the coupling between MUT and microwave source. Note that, experimental measurements as well as computer simulations of the in-plane incident microwave field created by the WR-90 rectangular waveguide at the MUT position showed that the formed field has a sufficiently high axial symmetry, and the radial distribution of the beam pattern is almost Gaussian at 5 mm distance from the end of the waveguide where the MUT was placed. The same dependence on the rotation angle was observed also in the numerical calculations when the graphite microstrip was radiated by a microwave field with Gaussian distribution which confirms that the phenomenon is not caused by the specificity of the radiated field of the waveguide.

3.2. Phase shift of microwave response

As mentioned above, the feature of the MMNF distribution for the MUT with different conductivity is caused by the phase shift between incident and scattered EM field. For the given parameters, the thickness of the graphite microstrip is significantly less than the thickness of the skin depth, thus, the approximation of the given field can be used. Nevertheless, since the real and imaginary parts
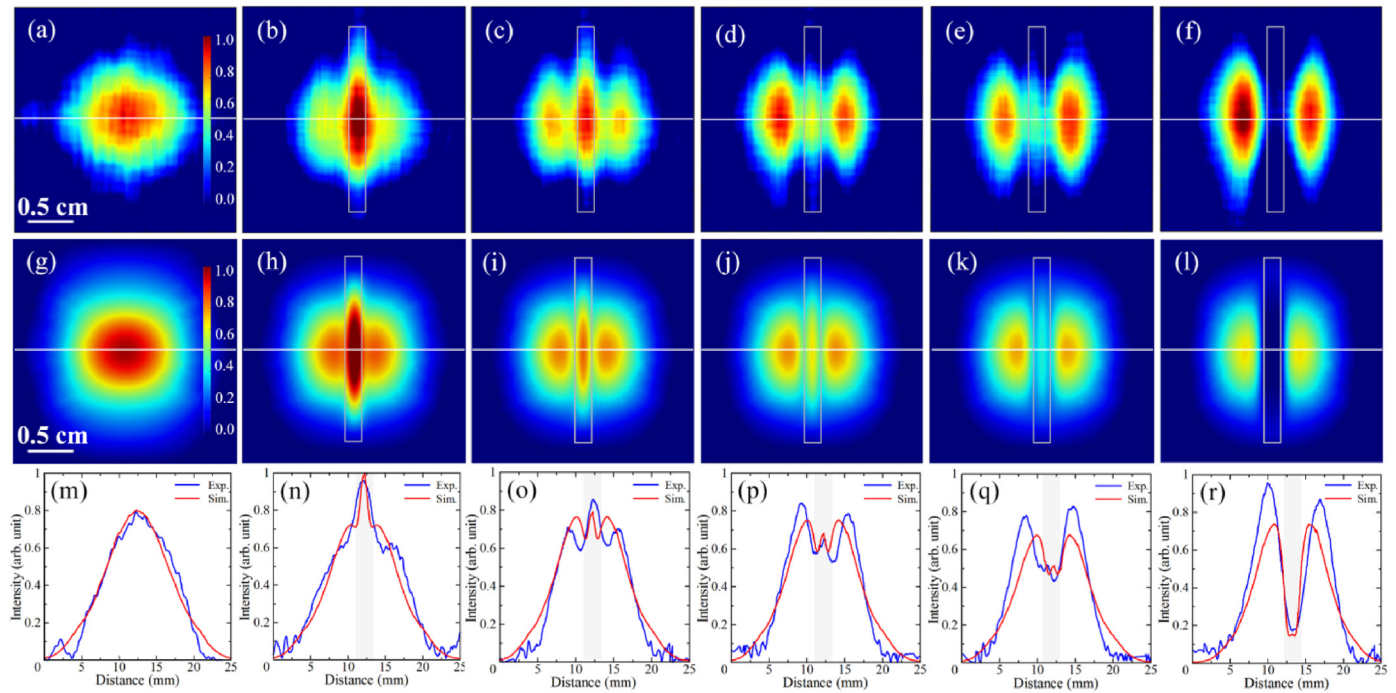
Fig. 2. The distribution of (a) measured and (g) simulated incident linear polarized microwave field 11 GHz (i.e. without MUT). The distributions of (b–f) measured and (h–l) simulated MMNF around the graphite microstrip at a distance of 1 mm from MUT with the different resistance: (b) 3.0 KOhm, (c) 1.3 KOhm, (d) 1.0 KOhm, (e) 0.8 KOhm, (f) 0.6 KOhm and conductivities: (h) 10 S/m, (i) 60 S/m, (j) 80 S/m, (k) 120 S/m, (l) 250 S/m. The grey rectangle represents the contour of the graphite microstrip. (m–r) Comparison of cross-sectional profiles for measured and simulated MMNF images are along white solid lines. (A colour version of this figure can be viewed online.)

of the MUT dielectric permittivity are of the same magnitude, the scattered field is shifted in phase and a distribution of MMNF was formed due to superposition of incident and scattered waves. It is noteworthy that the formation and transformation of the curves in Fig. 2(n–r) can be explained by the change in the conductivity of the microstrip, which results in the shift of the scattered EM field phase. To verify this, we analyze the distribution of the resulting magnetic field at a distance of d, along x-axis, perpendicular to the microstrip, Fig. 3(a). The incident (H_I) and scattered (H_S) magnetic fields (directed along x-axis) can be described by the following expressions:

$$H_I = H_0 e^{-\alpha x^2} e^{i\omega t},$$

$$H_S = \beta H_0 e^{i(\omega t + \varphi)} G(x). \tag{1}$$

Here α and β characterize the incident field distribution and its transformation to the scattered field respectively, H_0 and ω are the amplitude and frequency of the incident magnetic field with Gaussian distribution, φ is the phase shift of the scattered field, and $G(x)$ is the normalized distribution of the scattered field along x-axis, where scattered field is represented as a sum (integral) of
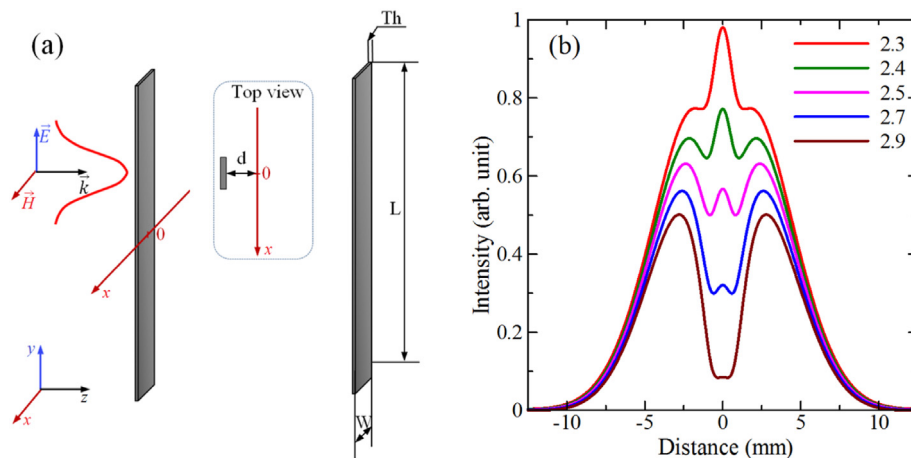

Fig. 3. (a) Schematic representation of the interaction between the microstrip and external EM field. The incidence EM field is linearly polarized along the y−axis (along the microstrip), propagates along the z−axis, and has a Gaussian distribution in the xy plane, the operating frequency $f = 11$ GHz ($\lambda = 2.7$ cm). The geometric characteristics of the conductive layer were set as follows: $L = 2$ cm, $W = 2$ mm, and $Th = 20$ μm. (b) In-plane distribution of MMNF along x−axis for $\alpha = 10^{-3}$ mm^{-2}, $\beta = 1$ and phase shift of $\varphi = 2.3$; $2.4; 2.5; 2.7; 2.9$ radians. (A colour version of this figure can be viewed online.)
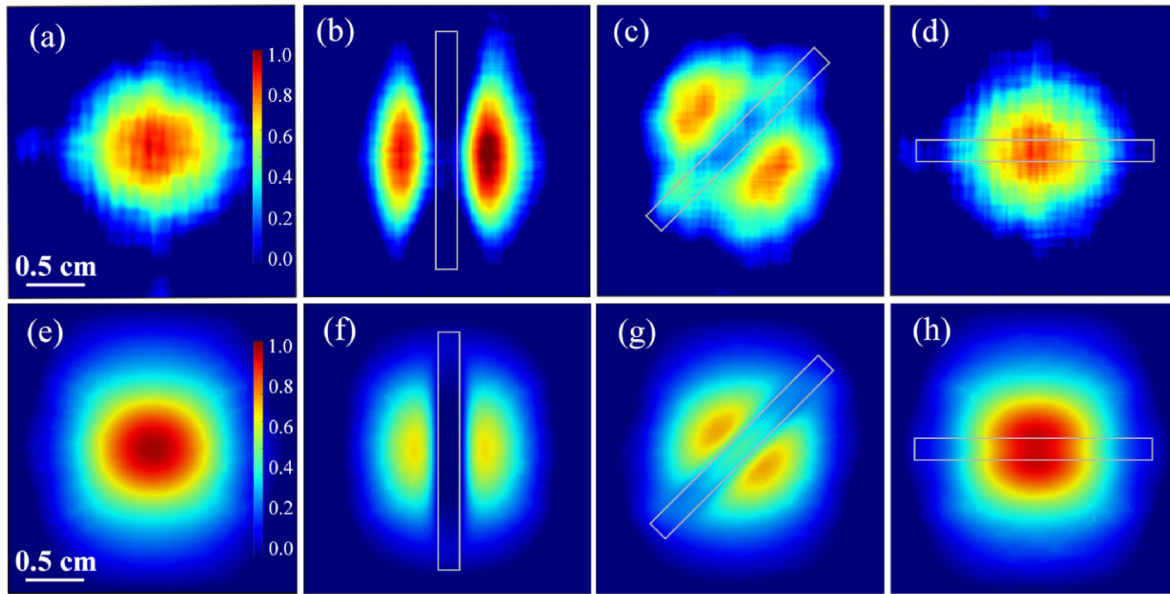
Fig. 4. The distribution of (a) measured and (e) simulated incident linear polarized MMNF with a 1 W intensity at 11 GHz (i.e. without MUT). In- plane distributions of (b–d) measured and (f–h) simulated MMNF around the graphite microstrip at a distance of 1 mm from MUT with the different orientations between MMNF polarization and microstrip: (b) and (f) 0°, (c) and (g) 45°, (d) and (h) 90°. The distance between microwave source and OI was fixed at 5 mm for all cases. The grey rectangle represents the contour of the graphite microstrip. (A colour version of this figure can be viewed online.)

magnetic fields scattered from single current-carrier rods:

$$G(x) = \frac{J(x)}{J(0)},$$

$$J(x) = \int_{-W/2}^{W/2} \frac{dx'}{\sqrt{(x - x')^2 + d^2}} = arsinh\left(\frac{2x + W}{2d}\right)$$
$$- arsinh\left(\frac{2x - W}{2d}\right). \qquad (2)$$

Then the profile of magnetic field along *x*-axis is described by the following expressions

$$Y(x) = \left|\frac{H_I + H_S}{H_0}\right|^2 = \left|e^{-\alpha x^2} + \beta e^{i\varphi}G(x)\right|^2. \qquad (3)$$

Note that $Th \ll W \ll L$ in the case under discussion (Fig. 3(a)).

Fig. 3(b) shows the magnetic field distribution according to the Y(x) function (Eq. (3)) for different phase shifts in the range of 2.3—2.9 radians. The similarity of these curves with graphs in Fig. 2(n—r) is obvious. This fact makes us to claim that changing the conductivity of the microstrip makes possible to control the phase shift of its response. In the future this circumstance will allow to create a phased array system for radiation front control based on metamaterial elements with regulated conductivity [33]. Though, it is worth to mention that absorption by the MUT may interfere with the precise execution of the expected processes. However, in such highly oriented structures, the role of absorption is important when the MUT length is much shorter than the wavelength of the incident EM wave [34]. In the case under consideration these values are of the same order ($L \sim \lambda$), thus the role of absorption is not significant. The numerical calculation shows that the microwave absorption by the MUT is small and does not significantly affect the phenomenon discussed. This is also confirmed by the similarity of curves trends in Fig. 2(n—r) and Fig. 3 (b). The last one is correct only within the approximation of the given field when absorption is neglected.

3.3. Polarization control

Additional information of angular behavior for interaction of incident EM field with MUT can be obtained by investigating the rotation of the microstrip axis at different angles.

In Fig. 4 the visualization of MMNF distributions with different angular (0°—90°) orientations of microstrip regarding to polarization of incident microwave radiation are shown at 11 GHz obtained with (b—d) experimental and (f—h) simulation methods. The resistance of graphite microstrip was 0.6 KOhm in the experiment and the conductivity of graphite microstrip was 250 S/m in simulation.

As follows from the previous analysis, in the case of $\vartheta = 0^0$ the presence of a dark zone in the central region of MMNF (Fig. 4 (b,f)) is due to the scattered wave phase shift by π compared with the incident wave. Herewith, the tangential components of these wave fields are equal in magnitude. The situation is quite different in the case of $\vartheta = 90^0$ (Fig. 4 (d,h)), which does not differ significantly from the case of the absence of a MUT (Fig. 4 (a,e)). Thus, the vertical component of a current-generating electric field does not change the distribution of MMNF. In the case of $\vartheta = 45^0$ (Fig. 4 (c,g)), the field also appears in the central part of the image. This shows that in this case only the component of the incident electric field parallel to the microstrip interacts with the MUT. As a result, the scattered field is smaller and does not compensate the incident field and confirms that distribution of the MMNF was formed due to superposition of incident and scattered waves.

Mechanisms of absorption, reflection, and transmission depend on the incident wave polarization and material characteristics (complex dielectric permittivity, conductivity, geometry, sizes, etc.) of the MUT. Thus, a graphite microstrip can be used as a controllable microwave and terahertz polarizer due to the angular—dependent behavior of the system [29,35,36].

4. Conclusion

In summary, TEOIM visualization technique was used to characterize the microwave response from MUT consisting of low-

conductive, graphite microstrip of limited length with different concentrations of carbon-resin mixtures. A significant change in the magnetic near-field distribution was observed due to a change in the conductivity of the graphite microstrip. Based on the similar results of the numerical calculation and computer simulation, the ratio of the real (ε_r) and imaginary (ε_i) parts of the effective dielectric permittivity ($\varepsilon = \varepsilon_r + i\varepsilon_i$) was highlighted. When $\varepsilon_i \ll \varepsilon_r$ the MMNF is mainly localized in the center of the microstrip, and with increasing of ε_i ($\varepsilon_i \rightarrow \varepsilon_r$) the MMNF is concentrated near the edges of microstrip. Theoretical analysis shows that the change in the field distribution is mainly caused by a significant change in the scattered microwave field phase, i.e. by changing the conductivity of the microstrip; the shift of the response phase from it can be controlled.

According to the obtained results, the MMNF spatial distribution strongly depends on the conductivity of the graphite microstrip and polarization of the incident microwave radiation. The phenomenon will provide a new opportunity to expand the properties of metamaterials particularly in creation of phased arrays for radiation front control based on metamaterial elements with regulated conductivity and will allow investigation of EM characteristics of low-conductive composite materials by a non-contact method.

CRediT authorship contribution statement

Arsen Babajanyan: Conceptualization, Methodology, Writing − original draft, Writing − review & editing. **Tigran Abrahamyan:** Methodology, Investigation. **Hovhannes Haroyan:** Software, Investigation, Writing − review & editing. **Billi Minasyan:** Investigation, Visualization. **Torgom Yezekyan:** Software, Writing − review & editing. **Kiejin Lee:** Methodology, Writing − review & editing. **Barry Friedman:** Writing − review & editing. **Khachatur Nerkararyan:** Conceptualization, Formal analysis, Writing − original draft.

Declaration of competing interest

The authors declare that they have no known competing financial interests or personal relationships that could have appeared to influence the work reported in this paper.

Acknowledgements

References

[1] P. Yu, L.V. Besteiro, Y. Huang, J. Wu, L. Fu, H.H. Tan, Ch Jagadish, G.P. Wiederrecht, A.O. Govorov, Zh Wang, Broadband metamaterial absorbers, Adv. Opt. Mater. 7 (3) (2019), 1800995.

[2] L. Aobo, Sh Singh, D. Sievenpiper, Metasurfaces and their applications, Nanophotonics 7 (6) (2018) 989−1011.

[3] S. Jahani, Z. Jacob, All-dielectric metamaterials, Nat. Nanotechnol. 11 (2016) 23−26.

[4] C.M. Soukoulis, M. Wegener, Past achievements and future challenges in 3D photonic metamaterials, Nat. Photonics 5 (2011) 523−530.

[5] A.M. Shaltout, V.M. Shalaev, M.L. Brongersma, Spatiotemporal light control with active metasurfaces, Science 364 (6441) (2019), eaat3100.

[6] D. Fei, Y. Yang, R.A. Deshpande, S.I. Bozhevolnyi, A review of gap-surface plasmon metasurfaces: fundamentals and applications, Nanophotonics 7 (6) (2018) 1129−1156.

[7] H.-H. Hsiao, ChH. Chu, D.P. Tsai, Fundamentals and applications of metasurfaces, Small Methods 1 (4) (2017), 1600064.

[8] Ch Hou-Tong, A.J. Taylor, N. Yu, A review of metasurfaces: physics and applications, Rep. Prog. Phys. 79 (2016), 076401.

[9] F. Bayatpur, K. Sarabandi, Single-layer high-order miniaturized-element frequency-selective surfaces, IEEE Trans. Microw. Theor. Tech. 56 (4) (2008) 774−781.

[10] G. Si, Y. Zhao, H. Liu, S. Teo, M. Zhang, T.J. Huang, A.J. Danner, J. Teng, Annular aperture array based color filter, Appl. Phys. Lett. 99 (2011), 033105.

[11] G. Si, Y. Zhao, E.S.P. Leong, J. Lv, Y.J. Liu, Incident-angle dependent color tuning from a single plasmonic chip, Nanotechnology 25 (2014), 455203.

[12] J. McVay, N. Engheta, A. Hoorfar, High impedance metamaterial surfaces using Hilbert-curve inclusions, IEEE Microw. Wireless Compon. Lett. 14 (3) (2004) 130−132.

[13] Z. Bayraktar, J.P. Turpin, D.H. Werner, Nature-inspired optimization of high-impedance metasurfaces with ultrasmall interwoven unit cells, IEEE Antennas Wirel, Propag. Lett. 10 (2011) 1563−1566.

[14] G.Y. Si, E.S.P. Leong, W. Pan, C.C. Chum, Y.J. Liu, Plasmon-induced transparency in coupled triangle-rod arrays, Nanotechnology 26 (2) (2014), 025201.

[15] T. Siday, P.P. Vabishchevich, L. Hale, C.T. Harris, T.S. Luk, J.L. Reno, O. Mitrofanov, Terahertz detection with perfectly-absorbing photoconductive metasurface, Nano Lett. 19 (5) (2019) 2888−2896.

[16] M. Khorasaninejad, Z. Shi, A.Y. Zhu, W.T. Chen, V. Sanjeev, A. Zaidi, F. Capasso, Achromatic metalens over 60 nm bandwidth in the visible and metalens with reverse chromatic dispersion, Nano Lett. 17 (3) (2017) 1819−1824.

[17] X.Z. Chen, L.L. Huang, H. Mühlenbernd, G.X. Li, B.F. Bai, Q. Tan, G. Jin, C.-W. Qiu, Sh Zhang, T. Zentgraf, Dual-polarity plasmonic metalens for visible light, Nat. Commun. 3 (2012), 1198.

[18] M.Q. Mehmood, S.T. Mei, S. Hussain, K. Huang, S.Y. Siew, L. Zhang, T. Zhang, X. Ling, H. Liu, J. Teng, A. Danner, Sh Zhang, Ch-W. Qiu, Visible-frequency metasurface for structuring and spatially multiplexing optical vortices, Adv. Mater. 28 (13) (2016) 2533−2539.

[19] J. Zhang, Zh Li, L. Shao, F. Xiao, W. Zhu, Active modulation of electromagnetically induced transparency analog in graphene-based microwave metamaterial, Carbon 183 (2021) 850−857.

[20] Y. Zhang, Y. Feng, J. Zhao, Graphene-enabled tunable multifunctional metamaterial for dynamical polarization manipulation of broadband terahertz wave, Carbon 163 (2021) 244−252.

[21] W. Hong, P. Xiao, H. Luo, Zh Li, Microwave axial dielectric properties of carbon fiber, Sci. Rep. 5 (2015), 14927.

[22] H.H. Ardakani, A. Mehrdadian, K. Forooraghi, Analysis of graphene-based microstrip structures, IEEE Access 5 (2017) 20887−20897.

[23] R. Moucka, S. Gona, M. Sedlacik, Accurate measurement of the true plane-wave shielding effectiveness of thick polymer composite materials via rectangular waveguides, Polymers 11 (2019) 1603.

[24] S. Karimkashi, D. Kajfez, A.A. Kishk, Sh Vaidya, Microwave conductivity measurements of carbon veil by two different methods, Microw. Opt. Technol. Lett. 51 (10) (2009) 2435−2438.

[25] G. Gradoni, D. Micheli, V. Mariani Primiani, F. Moglie, M. Marchetti, Determination of the electrical conductivity of carbon/carbon at high microwave frequencies, Carbon 54 (2013) 76−85.

[26] D. Zhang, Z. Hao, Y. Qian, Y. Huang, Bizeng, Zh Yang, W. Qibai, Simulation and measurement of optimized microwave reflectivity for carbon nanotube absorber by controlling electromagnetic factors, Sci. Rep. 7 (2017) 479.

[27] A. Bunde, W. Dieterich, Percolation in composites, J. Electroceram. 5 (2000) 81−89.

[28] Z. Rimska, V. Kresalek, J. Spacek, AC conductivity of carbon fiber-polymer matrix composites at the percolation threshold, Polym. Compos. 23 (1) (2002) 95−103.

[29] R. Kumar, S. Sahoo, E. Joanni, R.K. Singh, W.K. Tan, K.K. Kar, A. Matsuda, Recent progress on carbon-based composite materials for microwave electromagnetic interference shielding, Carbon 177 (2021) 304−331.

[30] H. Lee, Sh Arakelyan, B. Friedman, K. Lee, Temperature and microwave near field imaging by thermo-elastic optical indicator microscopy, Sci. Rep. 6 (2016), 39696.

[31] H. Lee, Zh Baghdasaryan, B. Friedman, K. Lee, Electrical defect imaging of ITO coated glass by optical microscope with microwave heating, IEEE Access 7 (2019) 42201−42209.

[32] Zh Baghdasaryan, A. Babajanyan, L. Odabashyan, Sh Arakelyan, H. Lee, G. Berthiau, B. Friedman, K. Lee, Thermal distribution in unidirectional carbon composite material due to the direct heating and microwave influence visualized by a thermo-elastic optical indicator microscope, Measurement 151 (2020), 107189.

[33] S.B. Glybovski, S.A. Tretyakov, P.A. Belov, Y.S. Kivshar, C.R. Simovski, Metasurfaces: from microwaves to visible, Phys. Rep. 634 (2016) 1−72.

[34] H. Parsamyan, H. Haroyan, Kh Nerkararyan, Broadband microwave absorption based on the configuration resonance of wires, Appl. Phys. A 126 (2020) 773.

[35] Sh Liu, Sh Qin, Y. Jiang, P. Song, H. Wang, Lightweight high-performance carbon-polymer nanocomposites for electromagnetic interference shielding, Composites A 145 (2021), 106376.

[36] N. Wu, Q. Hu, R. Wei, X. Mai, N. Naik, D. Pan, Zh Guo, Zh Shi, Review on the electromagnetic interference shielding properties of carbon based materials and their novel composites: recent progress, challenges and prospects, Carbon 176 (2021) 88−105.